

See discussions, stats, and author profiles for this publication at: <https://www.researchgate.net/publication/263941262>

Bi₂O₃–Bi₂WO₆ Composite Microspheres: Hydrothermal Synthesis and Photocatalytic Performances

ARTICLE *in* THE JOURNAL OF PHYSICAL CHEMISTRY C · MARCH 2011

Impact Factor: 4.77 · DOI: 10.1021/jp108414e

CITATIONS

100

READS

53

5 AUTHORS, INCLUDING:



Yafei Li

Nanjing Normal University

48 PUBLICATIONS 2,049 CITATIONS

SEE PROFILE



Zhen Zhou

Nankai University

213 PUBLICATIONS 6,990 CITATIONS

SEE PROFILE



Wei Chen

Nankai University

21 PUBLICATIONS 650 CITATIONS

SEE PROFILE

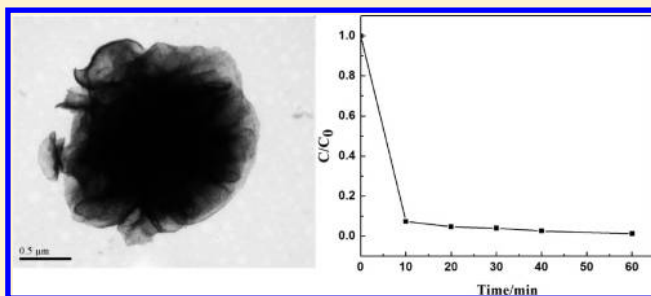
Bi₂O₃–Bi₂WO₆ Composite Microspheres: Hydrothermal Synthesis and Photocatalytic Performances

Ming Ge,[†] Yafei Li,[‡] Lu Liu,[†] Zhen Zhou,^{*,‡} and Wei Chen^{*,†}

[†]Tianjin Key Laboratory of Environmental Remediation and Pollution Control, [‡]Institute of New Energy Material Chemistry, and Key Laboratory of Advanced Energy Materials Chemistry (Ministry of Education), Nankai University, Tianjin 300071, P. R. China.

Supporting Information

ABSTRACT: Chrysanthemum-analogous Bi₂O₃–Bi₂WO₆ composite microspheres, assembled by nanosheets, were synthesized through a one-step hydrothermal route with the aid of surfactant templates. X-ray diffraction (XRD), X-ray photoelectron spectroscopy (XPS), scanning electron microscopy (SEM), and transmission electron microscopy (TEM) were employed to clarify the structure and morphology of the Bi₂O₃–Bi₂WO₆ microspheres. Nitrogen adsorption and desorption isotherms were conducted to examine the specific surface area and the pore nature of the as-prepared microspheres. The photocatalytic activity of the Bi₂O₃–Bi₂WO₆ composite microspheres was evaluated by using rhodamine B as a model contaminant, and over 99% of rhodamine B was degraded within 10 min under the exposure of sunlight. The Bi₂O₃–Bi₂WO₆ composite microspheres presented enhanced photocatalytic performances compared with separate Bi₂O₃, Bi₂WO₆, and conventional P25.



1. INTRODUCTION

Numerous efforts have been made to develop highly effective photocatalysts for the photodecomposition of waterborne contaminants. Currently, TiO₂ is the most commonly used photocatalyst; however, TiO₂ with large band gap can only exhibit high photocatalytic activity under ultraviolet (UV) light, which significantly limits its practical applications. Recently, synthesis of photocatalysts effective in contaminant decomposition under visible light irradiation has become an area of growing interest. Some of the most noteworthy materials include TiO₂ doped with C, N, B,¹ or rare earth elements.²

Bi₂WO₆ and Bi₂O₃ have advantage over TiO₂ in the visible light range. Bi₂WO₆ is a typical aurivillius oxide—Bi₂A_{n-1}B_nO_{3n+3} (A = Ca, Sr, Ba, Pb, Na, K, and B = Ti, Nb, Ta, Mo, W, Fe, when *n* = 1)—that possesses excellent intrinsic physical and chemical properties due to its layered structure.^{3,4} It has been reported that both Bi₂WO₆ nanostructures and microstructures show relatively high photocatalytic activity for the degradation of rhodamine B (RhB) under visible light irradiation.^{5–8} Bi₂O₃ is a p-type semiconductor with a band gap of ~2.8 eV.⁹ As a photocatalyst, this value accounts for its ability to oxidize water and possibly generate highly reactive species, such as O₂^{•-} and OH[•] radicals, which may act as initiators of oxidation reactions.¹⁰ Though Bi₂WO₆ and Bi₂O₃ have shown promise as novel photocatalysts, their efficiencies under visible light need to be improved for the more cost-effective removal of specific organic contaminants.¹⁰ Recently, the composite semiconductor photocatalysts have received great attention due to their enhanced

photocatalytic activities.^{11–14} In composite semiconductors, some advantages can be achieved: an improvement of charge separation, an increase in the lifetime of the charge carrier, and an enhancement of the interfacial charge transfer efficiency to adsorbed substrate.¹⁵ Moreover, an emerging research area in photocatalysis is the synthesis of three-dimensional (3D) nanostructures with individual nanocrystals as building blocks. Compared with conventional materials, the 3D nanostructures have several advantages, such as the profitability of size-quantized, nanometer-sized semiconductor particles with higher redox potentials as a result of the increase in band gap energy, which helps to retain high catalytic activities. Furthermore, the larger diameters of 3D microspheres allow easier separation and recycling of the materials in water treatment.^{16–18}

Herein, we report the synthesis of 3D Bi₂O₃–Bi₂WO₆ composite microspheres (composed of nanosheets) through a hydrothermal route with surfactant cetyltrimethylammonium bromide (CTAB) as the template. This method is simple and mild, and it is possible to control the 3D curved morphology of composite superstructures through a one-step route. The photocatalytic performances of the 3D composite microspheres were evaluated by examining the degradation of RhB.

Received: September 3, 2010

Revised: January 5, 2011

Published: March 07, 2011

2. EXPERIMENTAL AND COMPUTATIONAL SECTION

2.1. Synthesis of Bi_2O_3 – Bi_2WO_6 Composite Microspheres.

All chemicals were analytical grade and used as received without further purification. The Bi_2O_3 – Bi_2WO_6 composite was synthesized via a hydrothermal process. In a typical experiment, 0.3 g of Na_2WO_4 and 0.6 g of surfactant CTAB were first dissolved in 10 mL of distilled water, and then 0.789 g of $\text{Bi}(\text{NO}_3)_3 \cdot 5\text{H}_2\text{O}$ was added slowly to the solution. The solution was stirred and sonicated for 10 min, until a white precipitate formed. Afterward, the precipitate was transferred to a 50 mL Teflon-lined autoclave, and the autoclave was filled with water to 80% of its total volume. The autoclave was then heated at 150 °C for 24 h and was allowed to cool to room temperature. The products in the autoclave were collected and washed with deionized water and pure ethanol and then dried in the air and stored for further use. The details of the synthesis of pure Bi_2WO_6 and pure Bi_2O_3 are presented in the Supporting Information.

2.2. Characterization. X-ray diffraction (XRD) spectra were obtained with a Rigaku Rotaflex diffractometer equipped with a rotating anode, by using $\text{Cu K}\alpha$ radiation over the range of $3^\circ \leq 2\theta \leq 80^\circ$. Scanning electron microscopy (SEM) images were obtained with a JEOL JSM-6700F field-emission SEM. Transmission electron microscopy (TEM) images were obtained with a JEOL JEM-2100F field-emission electron microscope. Nitrogen adsorption and desorption experiments were conducted at 77.35 K with a Micromeritics Tristar 3000 analyzer. The Brunauer–Emmett–Teller (BET) surface area was estimated by using the adsorption data. X-ray photoelectron spectroscopy (XPS) was conducted on an ESCALAB 250 photoelectron spectroscope (Thermo Fisher Scientific Inc.) by using $\text{Al K}\alpha$ radiation.

2.3. Photocatalytic Tests. (1) Photocatalytic activities were evaluated by examining the photodegradation of RhB under simulated sunlight irradiation by using a 350 W Xe lamp. The photodegradation experiments were conducted by using a cylindrical quartz reactor with water circulation facility. In each test, the catalyst (0.2 g) was added to 200 mL of RhB solution ($2 \times 10^{-5} \text{ mol L}^{-1}$). Before the photodegradation experiment was initiated, the suspension was magnetically stirred in the dark for 30 min. Once the photodegradation experiment started, 4 mL aliquots were collected at selected time intervals and were centrifuged to remove photocatalyst powders. The concentrations of RhB were analyzed by measuring the absorbance at 553 nm with a UV-2550 spectrophotometer (Shimadzu, Japan). (2) Photocatalytic activity was also examined through the degradation of RhB under sunlight in Tianjin in September, 2009. The reaction cell was placed in a 150 mL beaker. Bi_2O_3 – Bi_2WO_6 composite catalyst (0.2 g) was added to 100 mL of RhB solution ($1 \times 10^{-5} \text{ mol L}^{-1}$). Before exposure under the sunlight, the suspension was magnetically stirred in the dark for 30 min. Aliquots of 3 mL of the solution were withdrawn at given time intervals to analyze the concentrations of RhB, by measuring the absorbance at 553 nm with the UV-2550 spectrophotometer.

2.4. Computation. The density of states (DOS) of Bi_2WO_6 and Bi_2O_3 was computed by using a linear combination of atomic orbitals and the density functional theory (DFT) method implemented in the DMol³ package.¹⁹ We employed the PW91 functional²⁰ with the generalized gradient approximation (GGA) and double numerical basis with polarization function (DNP). The core electrons of W and Bi atoms were described by the all-electron relativistic method. The k -point sampling was employed within the Monkhorst–Pack scheme.

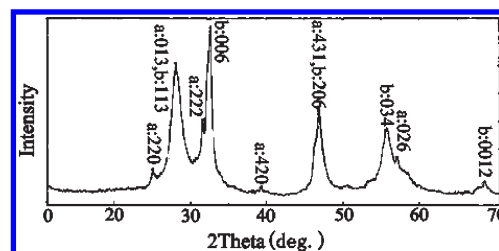


Figure 1. XRD patterns of the product: (a) Bi_2O_3 and (b) Bi_2WO_6 .

3. RESULTS AND DISCUSSION

3.1. Material Characterization. XRD was used to characterize the phase structure of the obtained product. Figure 1 shows the XRD pattern of the as-prepared Bi_2O_3 – Bi_2WO_6 composite microspheres. The XRD pattern indicates that the two types of crystals are in conformity with cubic Bi_2O_3 ($a = 10.08 \text{ \AA}$, JCPDS 74-1375, α - Bi_2O_3) and orthorhombic Bi_2WO_6 ($a = 5.457 \text{ \AA}$, $b = 5.436 \text{ \AA}$, $c = 16.427 \text{ \AA}$, JCPDS 73-1126). The characteristic peaks observed for α - Bi_2O_3 are assigned to the diffraction from the (220), (013), (222), (420), (431), and (026) planes. The characteristic peaks of Bi_2WO_6 correspond to the diffraction from the (113), (006), (206), (034), and (0012) planes. Therefore, the 3D composite microspheres are composed of Bi_2WO_6 and Bi_2O_3 . The XRD patterns of pure Bi_2WO_6 and Bi_2O_3 are shown in Figure S1 (see the Supporting Information).

The XPS spectra shown in Figure 2 give further evidence for the coexistence of Bi_2O_3 and Bi_2WO_6 in the obtained sample. The two peaks located at 35.5 and 37.8 eV are assigned to W4f .²¹ Another peak located at 529.9 eV is assigned to O1s . In general, the O1s peak is broad and complicated due to the nonequivalence of surface oxygen ions, and the simple peak shape comes from the overlapping contributions of oxide ions, that is, due to the O^{2-} of bismuth oxide. The binding energies for $\text{Bi4f}_{7/2}$ and $\text{Bi4f}_{5/2}$ are 158.9 and 164.4 eV, which can be attributed to Bi^{3+} and Bi^{4+} , respectively.^{22,23}

The low-magnification SEM image shows that the as-prepared sample is composed of many uniform, spherulike architectures ranging from 1 to 3 μm in diameter (Figure 3a). The high-magnification SEM images show that Bi_2O_3 – Bi_2WO_6 microspheres are built from small 2D crystalline nanosheets with thickness of $\sim 20 \text{ nm}$. These thin crystal sheets are aligned to the spherical surface, pointing toward a common center (Figure 3b and 3c), analogous to a chrysanthemum.

Figure 4a shows the TEM image of the Bi_2O_3 – Bi_2WO_6 nanosheet-based nanostructures. A typical TEM image of an isolated Bi_2O_3 – Bi_2WO_6 microsphere is shown in Figure 4b. The edge portion of the superstructure is lighter than that of the center and is comprised of sheetlike 2D nanostructures. The high-resolution TEM image of a single nanosheet in the microspheres (Figure 4c) shows the single crystalline structure. The lattice spacing of 0.271 nm corresponds to the d spacing between adjacent (006) crystallographic planes of Bi_2WO_6 , while the fringes of $d = 0.33 \text{ nm}$ match the (120) plane of α - Bi_2O_3 ; therefore, it can be confirmed that a $\text{Bi}_2\text{O}_3/\text{Bi}_2\text{WO}_6$ nanocrystal heterojunction formed in the composite.

BET gas sorptometry measurements were conducted to examine the porous nature of the Bi_2O_3 – Bi_2WO_6 microspheres. Figure 5 shows the N_2 adsorption/desorption isotherms and the pore size distribution (inset) of the Bi_2O_3 – Bi_2WO_6 microspheres. The isotherms are identified as type IV, which is the

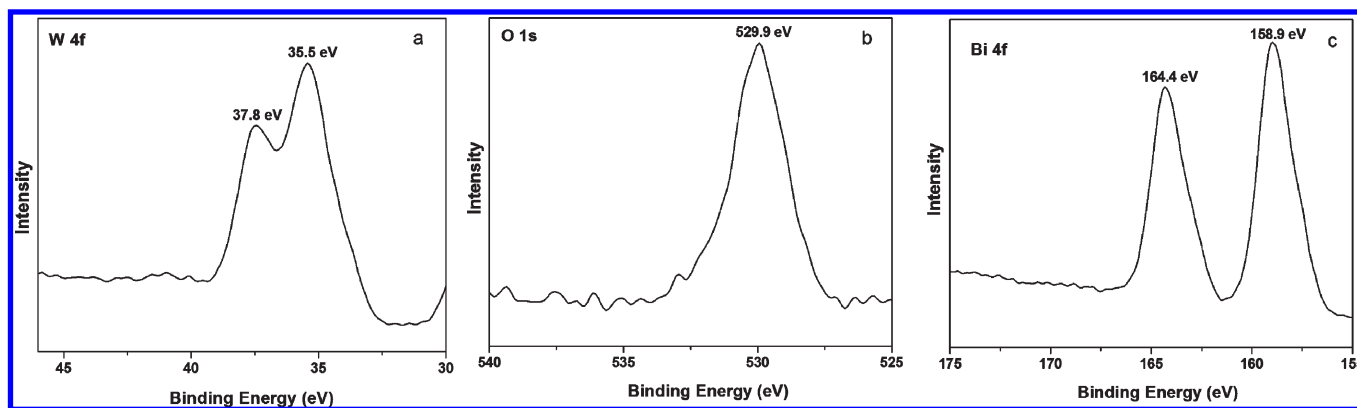


Figure 2. XPS spectra of Bi_2O_3 - Bi_2WO_6 composite microspheres.

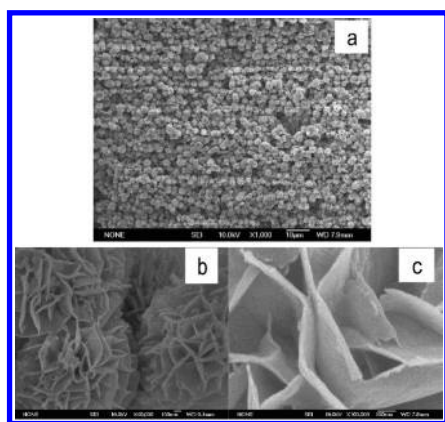


Figure 3. SEM images of Bi_2O_3 - Bi_2WO_6 composite: (a) low magnification; (b, c) high magnification.

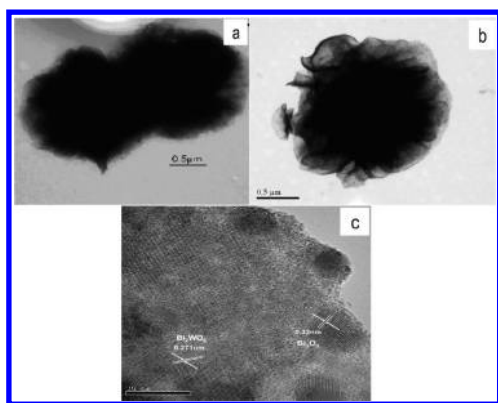


Figure 4. TEM images of Bi_2O_3 - Bi_2WO_6 microspheres.

characteristic isotherm of mesoporous materials. The pore size distribution data indicate that a majority of the pores are smaller than 5 nm. These pores presumably arise from the spaces among the nanosheets within the Bi_2O_3 - Bi_2WO_6 microspheres.²⁴ The BET surface area of the sample is $13.3 \text{ m}^2 \text{ g}^{-1}$. The single-point total volume of pores at $P/P_0 = 0.975$ is $0.51 \text{ cm}^3 \text{ g}^{-1}$. The BET surface area and the large total pore volume strongly indicate that the as-prepared microspheres have a mesoporous structure.

3.2. Formation Mechanism. To substantially understand the growth mechanism of the Bi_2O_3 - Bi_2WO_6 microspheres, the

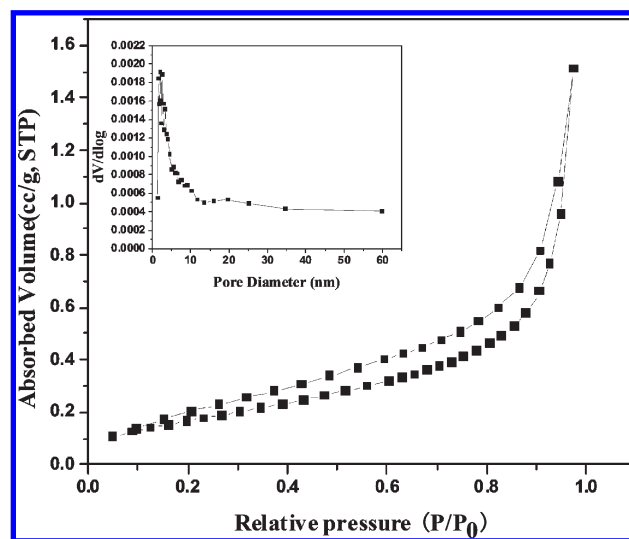


Figure 5. Nitrogen adsorption/desorption isotherm and Barrett-Joyner-Halenda (BJH) pore size distribution plot (inset) of Bi_2O_3 - Bi_2WO_6 microspheres.

products captured at different growth stages were analyzed by the SEM images in Figure 6. Initially (0.5 h), the product was composed of irregular flowers and particles (Figure 6a). After 1 h and 2 h of hydrothermal treatment, the amounts of irregular flower superstructure increased, accompanying the shape evolution from particles to flowers (Figure 6b and Figure 6c). After 4 h, only flower superstructures were found (Figure 6d), but they were not completely ripened. Finally, fully developed microsphere superstructures were obtained after hydrothermal treatment for 24 h (Figure 2).

Besides hydrothermal time, the reaction temperature also had a significant influence on the morphology of the as-synthesized products. When the hydrothermal temperature was 120°C , the product was composed of nanosheets with a trend to form microspheres (Figure S2a, Supporting Information). When the temperature increased to 180°C , the morphology of the product was not uniform; quasi-sphere particles and nanosheets were mixed (Figure S2b, Supporting Information). Irregular particles were found in the absence of surfactant CTAB (Figure S2c, Supporting Information), which reveals that surfactant CTAB was an important template to form Bi_2O_3 - Bi_2WO_6 microspheres.

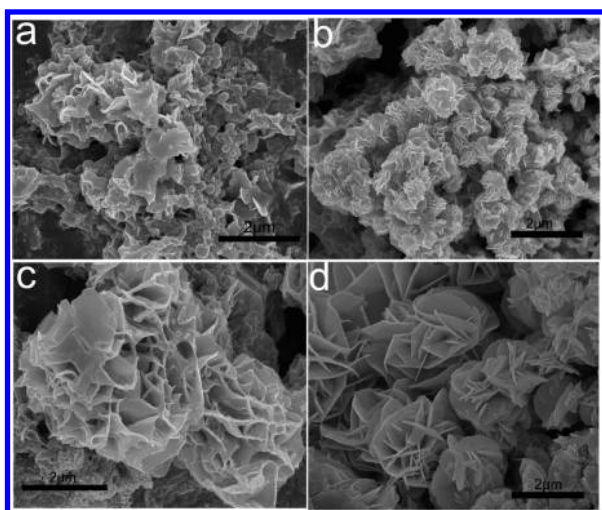


Figure 6. SEM images of the products at different synthetic times: (a) 0.5, (b) 1, (c) 2, and (d) 4 h.

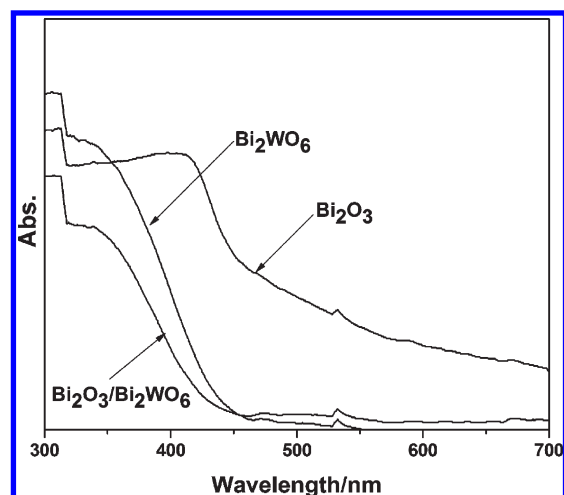


Figure 7. UV-vis absorption spectra of Bi_2O_3 , Bi_2WO_6 , and $\text{Bi}_2\text{O}_3/\text{Bi}_2\text{WO}_6$ composite.

When the surfactant is used, the surfactant molecules can cap on the crystal surface selectively. Generally, the face with a higher density of surface atoms is blocked during the growth of colloidal nanocrystals, and the growth along this facet is therefore considerably restricted.²⁵ In the synthetic process, the growth is inhibited in the direction perpendicular to the (113) crystal surface, resulting in flexible nanosheets that could readily intermesh each other to form a 3D porous structure.²⁶ Without any surfactant, the chrysanthemum-like 3D microspheres would not form. There are $(\text{CH}_3)_3(\text{C}_{16}\text{H}_{33})\text{N}^+$ functional groups on surfactant molecule, which provide complex sites for anions. Before synthetic reaction occurs, a lot of WO_4^{2-} ions gather on complex sites; these WO_4^{2-} anions react with Bi^{3+} and form the Bi_2WO_6 crystal nucleus. Then, these instantaneously formed Bi_2WO_6 nanoclusters in solution may attach to the Bi_2WO_6 nucleus on the complex sites, and the cluster gathers into colloidal spherical aggregates to minimize their surface area and decrease their energy. By random Brownian-motion-driven particle collisions, the spherical aggregates may further coagulate

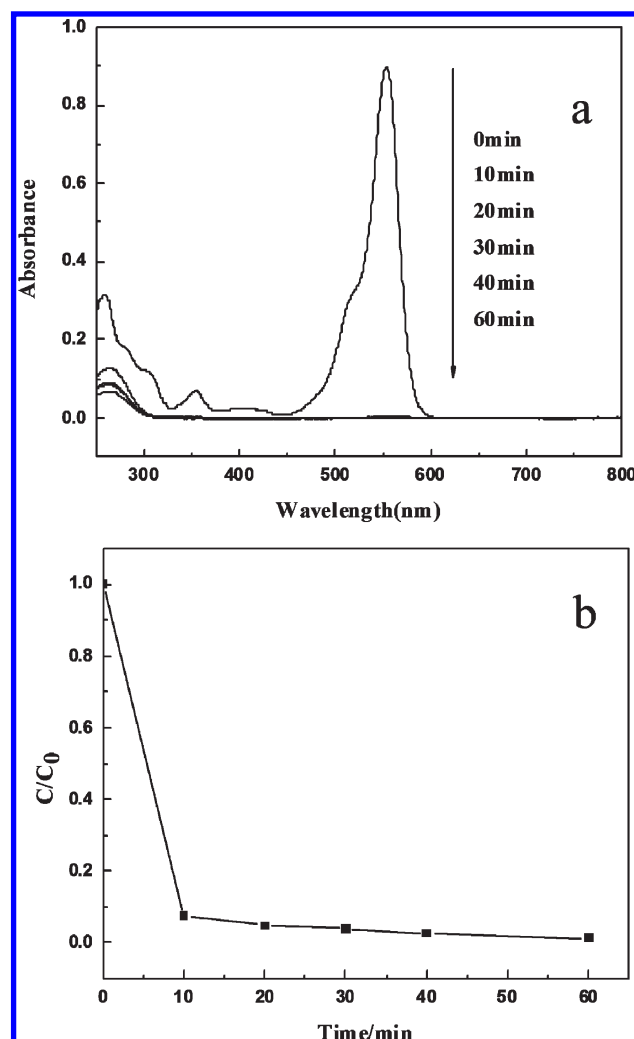


Figure 8. Photodecomposition of RhB ($C_0 = 10^{-5} \text{ mol L}^{-1}$) in the presence of $\text{Bi}_2\text{O}_3\text{--Bi}_2\text{WO}_6$ composite microspheres under the exposure to sunlight: (a) absorption spectrum of the RhB; (b) change of RhB concentration with time.

to form multimers.²⁷ Due to a supersaturated Bi_2WO_6 solution in their surroundings, the crystal growth is initiated preferentially from the most thermodynamically active clusters on the surface of the multimers.²⁸ The above surfactant molecules can cap on the crystal surface selectively, which leads to a limited growing direction. The Bi_2WO_6 nanosheets grow along the (006) and (206) crystallographic directions and are enclosed by (113) facets, i.e., the widest facets, as suggested in the XRD pattern. By means of the Ostwald ripening process, the exterior of the multimers forms nanosheets by self-assembly along (006) and (206) directions. As a result, the multimers are constructed into ordered nanosheet-based 3D microspheres. On the other hand, the synthetic reactions of Bi_2WO_6 serve as a striking illustration of the way that the outcome of a chemical reaction can be determined, in one instance, by rate of reactions, and by stabilities of the final products. In short reaction time, Bi_2WO_6 particle-shaped products predominate, and the reaction is under kinetic control or rate control. In long reaction time, sufficient energy is available for the products to hurdle their energy barrier to lead to Bi_2WO_6 microspheres, so such reaction is under thermodynamic control or equilibrium control. Similarly, Bi_2O_3

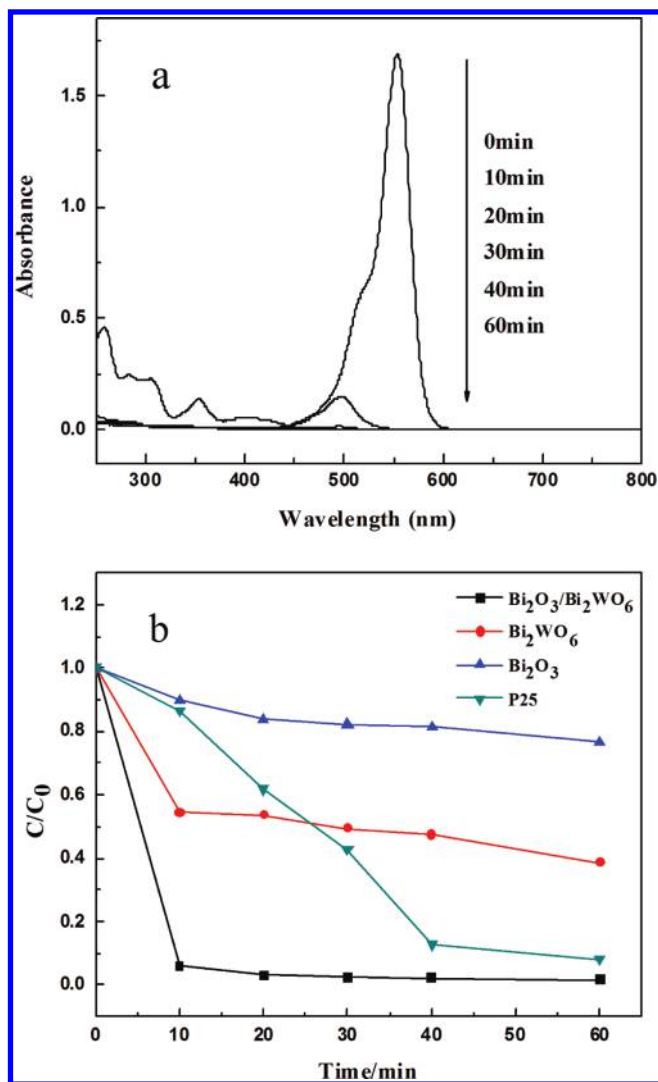


Figure 9. Photodecomposition results: (a) absorption spectrum of dissolved RhB ($2 \times 10^{-5} \text{ mol L}^{-1}$, 200 mL) in the presence of $\text{Bi}_2\text{O}_3\text{--Bi}_2\text{WO}_6$ composite; (b) comparison of photodegradation kinetics of dissolved RhB ($2 \times 10^{-5} \text{ mol L}^{-1}$, 200 mL) in the presence of different catalysts.

along (013) and (431) directions also coprecipitates with Bi_2WO_6 to form $\text{Bi}_2\text{O}_3\text{--Bi}_2\text{WO}_6$ composite microspheres.

3.3. Optical Properties and Photocatalytic Performances.

The room temperature UV–vis absorption spectra of pure Bi_2O_3 , Bi_2WO_6 , and $\text{Bi}_2\text{O}_3\text{--Bi}_2\text{WO}_6$ composite are shown in Figure 7. The band gaps (E_g) of these three products are estimated to be about 2.67, 2.97, and 2.98 eV, respectively, from the first derivative of the absorption edge, which indicates that these three catalysts absorb in the visible light range.

The photocatalytic activity of the 3D $\text{Bi}_2\text{O}_3\text{--Bi}_2\text{WO}_6$ composite microspheres under the sunlight was examined with RhB (with an initial concentration, C_0 , of $1 \times 10^{-5} \text{ mol L}^{-1}$) as the test contaminant, and the results are shown in Figure 8. The characteristic wavelength of RhB absorption is 553 nm, and the area of the absorption peak correlates well with the RhB concentration. As shown in the figure, the concentration of RhB decreased sharply with the exposure time, and over 99% of RhB was degraded within 10 min. In addition, no new absorption bands appear in either the visible or ultraviolet region.

The dosage effect of the $\text{Bi}_2\text{O}_3\text{--Bi}_2\text{WO}_6$ composite on the degradation of RhB was investigated under simulated sunlight irradiation. The results are shown in Figure S3 (see the Supporting Information). Obviously, the degradation efficiency increased with increasing photocatalyst dosage, due to the increase in the number of active sites available for the photocatalytic reaction. To further evaluate the photocatalytic activity of the $\text{Bi}_2\text{O}_3\text{--Bi}_2\text{WO}_6$ composite, the photodecompositions of RhB in the presence of different catalysts, including the $\text{Bi}_2\text{O}_3\text{--Bi}_2\text{WO}_6$ composite, Bi_2WO_6 , Bi_2O_3 , and Degussa P25 titania, were compared. The experiments were conducted under the exposure of simulated sunlight. Figure 9a shows the evolution of RhB absorption spectra in the presence of the $\text{Bi}_2\text{O}_3\text{--Bi}_2\text{WO}_6$ composite. The absorption peaks, corresponding to the characteristic adsorption of RhB at 553 nm, decreased rapidly with the increase of exposure time and completely disappeared in approximately 20 min. As shown in Figure 9b, the 3D $\text{Bi}_2\text{O}_3\text{--Bi}_2\text{WO}_6$ composite exhibits significantly greater efficiency in the photodecomposition of RhB than Bi_2O_3 , Bi_2WO_6 and the conventional photocatalyst P25.

3.4. Photocatalytic Mechanism. The remarkably high photocatalytic activity of the $\text{Bi}_2\text{O}_3\text{--Bi}_2\text{WO}_6$ composite under the sunlight is probably due to the difference between the conduction band edges of Bi_2O_3 and Bi_2WO_6 , which leads to irreversible charge transfer from one semiconductor to the other and therefore reduces the electron–hole recombination when photoexcitation occurs. Figure 10 shows the DOS for Bi_2O_3 and Bi_2WO_6 . For Bi_2WO_6 , the valence band maximum (VBM) has the O2p and Bi6s hybridization character, while the states of the conduction band minimum (CBM) are composed of W5d orbitals. The DOS indicates that charge transfer upon photoexcitation occurs from the O2p+Bi6s hybridization orbitals to the empty W5d orbitals. For Bi_2O_3 , the VBM is composed of O2p, Bi6s, and Bi6p hybridization, while the CBM is attributed to the hybridization orbitals of O2p and Bi6p. When photoexcitation starts, electrons from O2p, Bi6s, and Bi6p hybridized orbitals enter O2p and Bi6p hybridized orbitals, and photogenerated electron–holes form. In the $\text{Bi}_2\text{O}_3\text{--Bi}_2\text{WO}_6$ composite photocatalyst, Bi_2O_3 is a p-type semiconductor and exhibits stronger oxidation activity than Bi_2WO_6 . This allows Bi_2O_3 to scavenge Bi_2WO_6 electrons to stabilize the charge separation and prevent rapid recombination. It must be pointed out that the holes migrate much faster than electrons,²⁹ and an increase of the holes in Bi_2WO_6 and a decrease of holes in Bi_2O_3 are expected under light irradiation. These will reduce recombination of photogenerated electrons and holes in the Bi_2WO_6 phase. Therefore, electrons on the Bi_2O_3 surface and holes on the Bi_2WO_6 surface could participate in photocatalytic oxidation reactions to degrade RhB, resulting in the enhanced photocatalytic activity.

In addition, previous studies showed that a suitable conformation of pores allows light waves to penetrate deep inside the photocatalysts and leads to high mobility of charge.^{30,31} It is speculated that the emanative pores in the 3D $\text{Bi}_2\text{O}_3\text{--Bi}_2\text{WO}_6$ microspheres allow the penetration of light waves, RhB in solution deep into this photocatalyst, which may greatly promote the photocatalytic activity. Also, the $\text{Bi}_2\text{O}_3\text{--Bi}_2\text{WO}_6$ microspheres were assembled by nanosheets, which are beneficial for promoting the photocatalytic efficiency because more electron–holes could be separated, transfer to the surface, and react with RhB molecules.³² The 3D $\text{Bi}_2\text{O}_3\text{--Bi}_2\text{WO}_6$ composites are a heterogeneous photocatalyst with large particle sizes that can be easily recycled by a simple filtration step and avoid the second pollution.

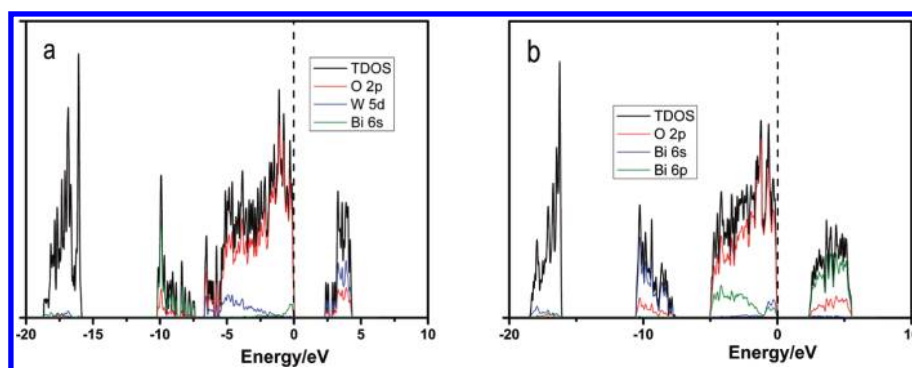


Figure 10. Density of states (DOS) of Bi_2WO_6 (a) and Bi_2O_3 (b) calculated through the DFT method.

4. CONCLUSION

In conclusion, we report a simple hydrothermal route to obtain the Bi_2O_3 – Bi_2WO_6 composite microspheres analogous to chrysanthemums, with diameters ranging from 1 to 3 μm , which are composed of nanosheets with thickness of 20 nm. Nearly complete (over 99%) photodegradation of RhB under the exposure of sunlight was achieved within 10 min with 3D Bi_2O_3 – Bi_2WO_6 composite microspheres as the photocatalyst. The excellent photocatalytic activity stems from the different conduction band edge positions of Bi_2O_3 and Bi_2WO_6 , which promote irreversible charge transfer from one semiconductor to the other; that is, Bi_2O_3 scavenges Bi_2WO_6 electrons, stabilizes the charge separation, and prevents rapid recombination.

■ ASSOCIATED CONTENT

Supporting Information. Detailed synthesis processes and XRD patterns of pure Bi_2WO_6 and Bi_2O_3 , SEM images of as-obtained products at various hydrothermal temperatures and without CTAB templates, and photodecomposition of RhB in the presence of Bi_2O_3 – Bi_2WO_6 composite microspheres with different dosages. This material is available free of charge via the Internet at <http://pubs.acs.org>.

■ AUTHOR INFORMATION

Corresponding Author

*E-mail zhouzhen@nankai.edu.cn (Z.Z.); chenwei@nankai.edu.cn (W.C.).

■ ACKNOWLEDGMENT

This work was supported by Ministry of Education (Grants 708020 and NCET 08-0293) and Ministry of Science and Technology (Grant 2009DFA91910) of China.

■ REFERENCES

- In, S.; Orlov, A.; Berg, R.; García, F.; Pedrosa-Jimenez, S.; Tikhov, M. S.; Wright, D. S.; Lambert, R. M. *J. Am. Chem. Soc.* **2007**, *129*, 13790.
- Xu, A. W.; Gao, Y.; Liu, H. Q. *J. Catal.* **2002**, *207*, 151.
- Zhang, C.; Zhu, Y. *Chem. Mater.* **2005**, *17*, 3537.
- Kim, N.; Vannier, R. N.; Grey, C. P. *Chem. Mater.* **2005**, *17*, 1952.
- Zhang, L. S.; Wang, W. Z.; Zhou, L.; Xu, H. L. *Small* **2007**, *3*, 1618.
- Fu, H. B.; Pan, C. S.; Yao, W. Q.; Zhu, Y. F. *J. Phys. Chem. B* **2005**, *109*, 22432.

- Zhang, C.; Zhu, Y. F. *Chem. Mater.* **2005**, *17*, 3537.
- Zhang, L. S.; Wang, W. Z.; Chen, Z. G.; Zhou, L.; Xu, H. L.; Zhu, W. J. *Mater. Chem.* **2007**, *17*, 2526.
- Xu, Y.; Schoonen, M. A. A. *Am. Mineral.* **2000**, *85*, 543.
- Hameed, A.; Montini, T.; Gombac, V.; Fornasiero, P. *J. Am. Chem. Soc.* **2008**, *130*, 9658.
- Shang, M.; Wang, W. Z.; Zhang, L.; Sun, S. M.; Wang, L.; Zhou, L. *J. Phys. Chem. C* **2009**, *113*, 14727.
- Zhang, L. S.; Wong, K. H.; Chen, Z. G.; Yu, J. C.; Zhao, J. C.; Hu, C.; Chan, C. Y.; Wong, P. K. *Appl. Catal., A* **2009**, *363*, 221.
- Long, M. C.; Cai, W. M.; Cai, J.; Zhou, B. X.; Chai, X. Y.; Wu, Y. H. *J. Phys. Chem. B* **2006**, *110*, 820211.
- Chai, S. Y.; Kim, Y. J.; Jung, M. H.; Chakraborty, A. K.; Jung, D.; Lee, W. I. *J. Catal.* **2009**, *262*, 144.
- Bessekhouad, Y.; Robert, D.; Weber, J.-V. *J. Photochem. Photobiol., A* **2004**, *163*, 569–580.
- Guo, C. S.; Ge, M.; Liu, L.; Gao, G. D.; Feng, Y. C.; Wang, Y. Q. *Environ. Sci. Technol.* **2010**, *44*, 419.
- Liu, L.; Liu, H. J.; Zhao, Y. P.; Wang, Y. Q.; Duan, Y. Q.; Gao, G. D.; Ge, M.; Chen, W. *Environ. Sci. Technol.* **2008**, *42*, 2342.
- Liu, Z. Y.; Sun, D. D.; Guo, P.; Leckie, J. O. *Chem.—Eur. J.* **2007**, *13*, 1851.
- (a) Delley, B. *J. Chem. Phys.* **1990**, *92*, 508. (b) Delley, B. *J. Chem. Phys.* **2000**, *113*, 7756.
- Perdew, J. P.; Wang, Y. *Phys. Rev. B* **1992**, *45*, 13244.
- Wu, J.; Duan, F.; Zheng, Y.; Xie, Y. *J. Phys. Chem. C* **2007**, *111*, 12866.
- Barreca, D.; Rizzi, F. M. G. A.; Scotti, R.; Tondello, E. *Phys. Chem. Chem. Phys.* **2001**, *3*, 1743.
- Morgan, W. E.; Stec, W. J.; van Wazer, J. R. *Inorg. Chem.* **1973**, *12*, 953.
- Hu, J. S.; Ren, L. L.; Guo, Y. G.; Liang, H. P.; Cao, A. M.; Wan, L. J.; Bai, C. L. *Angew. Chem.* **2005**, *117*, 1295.
- Si, R.; Zhang, Y. W.; You, L. P.; Yan, C. H. *Angew. Chem., Int. Ed.* **2005**, *44*, 3256.
- Yu, S. H.; Shu, L.; Yang, J.; Han, Z. H.; Qian, Y. T.; Zhang, Y. H. *J. Mater. Res.* **1999**, *14*, 4157.
- Kim, W. T.; Kim, C. D. *J. Appl. Phys.* **1986**, *60*, 2631.
- Liu, L.; Liu, H. J.; Kou, H. Z.; Wang, Y. Q.; Zhou, Z.; Ren, M. M.; Ge, M.; He, X. W. *Cryst. Growth Des.* **2009**, *9*, 113.
- Enright, B.; Fitzmaurice, D. *J. Phys. Chem.* **1996**, *100*, 1027.
- Bian, Z. F.; Zhu, J.; Wang, S. H.; Cao, Y.; Qian, X. F.; Li, H. X. *J. Phys. Chem. C* **2008**, *112*, 6258.
- Wang, X.; Yu, J. C.; Ho, C.; Hou, Y.; Fu, X. *Langmuir* **2005**, *21*, 2552.
- Hagfeldt, A.; Gratzel, M. *Chem. Rev.* **1995**, *95*, 49.